Electrochimica Acta 521 (2025) 145925

Contents lists available at ScienceDirect

Electrochimica Acta

journal homepage: www.journals.elsevier.com/electrochimica-acta

Corrosion of $TiHfZrNb_x$ high-entropy alloys in a simulated condition of proton exchange membrane water electrolyser

Mariya Kadiri [a], Ayoub Tanji [b], Xuesong Fan [c], Peter K Liaw [c], T M Indra Mahlia [d], Hendra Hermawan [a,*]

[a] Department of Mining, Metallurgical, and Materials Engineering, Laval University, Quebec City, QC G1 V 0A6, Canada
[b] Quebec Metallurgy Center, Trois-Rivières, QC G9A 5E1, Canada
[c] Department of Materials Science and Engineering, The University of Tennessee, Knoxville, TN 37996, USA
[d] Centre for Technology in Water and Wastewater, School of Civil and Environmental Engineering, Faculty of Engineering and Information Technology, University of Technology Sydney, Sydney, NSW 2007, Australia

ARTICLE INFO

Keywords:
Bipolar plate
Corrosion resistance
High-entropy alloy
Passive film
Proton exchange membrane water electrolysis

ABSTRACT

In the present work, the corrosion behavior and passive film properties of $TiHfZrNb_x$ ($x = 0.2$, 0.3 and 0.4) high-entropy alloys (HEAs) were evaluated under a simulated condition of a proton exchange membrane water electrolyser (PEMWE) in view of their application as bipolar plates. Results from electrochemical-impedance spectroscopy, cyclic- and static-polarizations evaluation revealed that in a 0.5 M H_2SO_4 + 5 ppm F^- solution at 70 °C the HEAs exhibited about 600 times higher polarization resistance than that of CP-Ti, with the highest achieved at 79.57 kΩ.cm^2 for $TiHfZrNb_{0.2}$, leading to a sharp contrast in the corrosion-current density, 805.11 μA.cm^{-2} for the CP-Ti vs. 0.92 μA.cm^{-2} for the $TiHfZrNb_{0.2}$, reflecting a far superior corrosion resistance of the HEAs. X-ray photoelectron spectroscopy analysis confirmed the formation of a multi-oxide passive film, predominantly by $HfO_2 > ZrO_2 > TiO_2$, with a presence of Nb_2O_5 only in $TiHfZrNb_{0.4}$, all possess an n-type semiconducting characteristic and a much lower electron-donor concentration in the HEAs than in the CP-Ti. The complementary analyses of scanning electron microscopy, atomic force microscopy and solution chemistry highlighted the synergistic effects of Hf, Zr, and Nb in enhancing protectiveness of the passive film, but the absence of Nb_2O_5 on the top surface of $TiHfZrNb_{0.2}$ and $TiHfZrNb_{0.3}$ indicated a small role of Nb toward passivation.

1. Introduction

The development of clean hydrogen production technologies has been receiving considerable attention and support, witnessed by an increasing number of projects and policies worldwide [1]. In the long term, hydrogen has a great potential to become an essential element of a clean, safe and cost-effective energy system of the future. Its versatility allows it to amplify the contribution of renewable energies, such as wind and solar photovoltaic matters, to the effort of mitigating climate change and protecting the environment [2]. High-purity and environmental friendly hydrogen has been produced through water electrolysis, particularly in proton exchange membrane water electrolyser (PEMWE) cells, where water molecules dissociate into hydrogen (H_2) and oxygen (O_2) under the influence of electricity from sustainable energy resources and with zero CO_2 emissions [3]. However, the short lifetime and high cost of PEMWE cells continue to be a major obstacle to their development and large-scale commercialization [4]. Among the damage factors that seriously reduce the performance and lifetime of this technology is the degradation of bipolar plates [5]. However, it receives insufficient attention compared to other components of a PEMWE cell, such as the catalytic layers for the hydrogen and oxygen evolution reactions at the cathode and anode [6,7].

The bipolar plates represent 30 % of the size and 50 % of the cost of a PEMWE cell, making it essential to design this component optimally [8]. They are located at the ends of each of the cells and have flow distribution channels that allow water to flow towards the catalytic membrane layer as well as for the evacuation of the generated gases. Currently, titanium (Ti) is often used as bipolar plates due to its light weight and higher corrosion resistance compared to stainless steels [9,10]. In a PEMWE cell, the bipolar plates are subjected to an acidic and

* Corresponding author.
E-mail address: hendra.hermawan@gmn.ulaval.ca (H. Hermawan).

https://doi.org/10.1016/j.electacta.2025.145925
Received 22 December 2024; Received in revised form 10 February 2025; Accepted 24 February 2025
Available online 25 February 2025

humid environment (pH of 2 - 4), a high operating temperature (70 - 80 °C), leaching of fluoride ions from the polymeric membrane, and a high electrode voltage (1.6 - 2 V in the anode part) [5,11]. This harsh environment can cause a breakdown of passive films and corrosion of the plates, which increases their surface contact resistance, thus reducing the overall efficiency of the cell [12]. At the same time, corrosion also causes metal dissolution, leading to a contamination of the catalytic sites and triggering a chemical degradation mechanism of the membrane. This process creates a chain reaction where membrane degradation releases fluoride ions that accelerate the corrosion of the bipolar plates, which leads to the metal ions dissolution that, in turn, catalyze the deterioration of the membrane, releasing more fluorides [11]. In addition, the accumulation of corrosion product deposits in the channels causes long-term obstruction and deformation of the channels, which leads to plate embrittlement [10]. Thus, understanding the degradation phenomena of these plates and finding alternative materials are crucial to developing more efficient and durable PEMWE cells.

Few works have proposed the coating of noble metals (Au, Pt, and Ir) on the corrosion resistance improvement of Ti bipolar plates [13]. However, in some cases, this protective coating expanded and delaminated after several hundred hours of operation, leading to the pollution of the catalytic membrane layer. Another work improved both corrosion resistance and surface conductivity of Ti alloys by adding Nb and Ta through matrix doping, indicating the potential benefit of multi-oxides passive films [14]. The limitations of using metals or alloys based mainly on a single element can be overcome using so-called high--entropy alloys (HEAs), novel alloys composed of several elements (5 elements and more) at equal concentrations. These alloys, characterized by their multi-element compositions, can exhibit unique properties such as superior hardness, high strength, and excellent wear resistance, making them highly attractive for applications in various fields, including thermoelectric and magnetocaloric materials, superconductors, and catalysis [15,16]. In the latter, HEAs possess a wide range of excellent qualities that distinguish them from conventional metal-based catalysts, including mechanical strength, thermostability, and radiation resistance. The stability and activity of HEA electrocatalysts have been demonstrated for the reaction of hydrogen-evolution and the oxygen-reduction reaction [17]. A refractory family of HEAs have recently been developed based on Ti, Zr, Hf, V, Nb, Ta, Mo, and W, resulting in a single BCC phase solid solution, and demonstrating an exceptional high-temperature behavior with remarkable resistance to oxidation and corrosion. They exhibited yield strengths ranging from 900 to 1600 MPa, while maintaining satisfactory compressive plasticity. In two previous works, we showed that a family of $TiZrHfNb_x$ HEAs exhibited higher corrosion resistance than Ti in chloride-containing solutions and revealed the role of Nb to the passivation/dissolution of passive films [18,19]. Therefore, the present work aims at determining the potential of $TiZrHfNb_x$ HEAs as alternative materials for PEMWE bipolar plates by thoroughly investigating their electrochemical-corrosion behavior in a solution of a 0.5 M H_2SO_4 with and without 5 ppm F^- at 70 °C. Through a series of electrochemical evaluations, including electrochemical impedance spectroscopy, cyclic potentiodynamic polarization, and potentiostatic polarization, combined with surface characterizations such as scanning electron microscopy, atomic force microscopy, and X-ray photoelectron spectroscopy, we aim to uncover the passivation and dissolution mechanisms of the HEAs. This will enhance the fundamental understanding of the corrosion behavior of bipolar plate materials under simulated PEMWE cell conditions.

2. Experimental

2.1. Sample preparation

Samples of $TiZrHfNb_x$ HEAs (x = 0.2, 0.3, and 0.4 in molar ratio, hereinafter referred to as $HEA_{0.2}$, $HEA_{0.3}$ and $HEA_{0.4}$) were prepared through arc melting of pure element mixtures (Ti, Zr, Hf, and Nb) in a Ti-gettered argon atmosphere. The ingots were solidified and remelted at least five times before being vacuum cast into a 6.35-mm diameter water-cooled copper mold and subsequently cut into thin rectangular plates, 2 mm thick. The microstructure of the produced HEAs is described in detail in other work [18]. Specimens for electrochemical evaluation were prepared from the HEAs and commercial pure titanium (CP-Ti), each having 1 cm^2 of the exposed surface embedded in an epoxy resin with copper-wire connections. Prior to each test, all specimen surface was polished with SiC paper up to 2400 grit, then with the 9-µm polycrystalline diamond suspension and 0.02-µm colloidal-silica suspension.

2.2. Electrochemical evaluation

The electrochemical evaluation was conducted using an electrochemical workstation (CH Instruments 760E, Austin, TX, USA) in a three-electrode cell system. The working electrode consisted of CP-Ti and HEA specimens, while a carbon rod served as the counter electrode, and a saturated calomel electrode (SCE) was used as the reference electrode. Therefore, all potential was referred to SCE. The electrolyte solution was a 0.5 M H_2SO_4 solution with and without 5 ppm F^-, by adjusting a proportion of NaF, and maintained at 70 °C ± 2 °C (with air bubbling) to simulate the anode side of a PEMWE cell. The electrochemical system was left to stabilize for 60 min at an open circuit potential (OCP). The electrochemical impedance spectroscopy (EIS) was performed using an applied AC amplitude of 10 mV, with 12 points per decade, over a scanning frequency range of 10^5 to 10^{-2} Hz. The cyclic-potentiodynamic polarization (CPP) was performed in a potential range of - 0.5 to + 2 V for the three HEA alloys and - 1 to + 2 V for CP-Ti, with a scan rate of 1 $mV.s^{-1}$. The potentiostatic polarization (PSP) was recorded at + 2 V for 2 h to ensure stable passive film formation. The Mott-Schottky was also conducted at potential ranges of - 1 to + 2 V for CP-Ti and from - 0.5 to + 2 V for HEAs, with a 10 $mV.s^{-1}$scanning rate. To ensure reproducibility, all experiments were conducted at least three times.

2.3. Surface characterization

Characterization of the passive film of CP-Ti and all HEA samples was performed before and at the end of the PSP test. A general surface morphology was observed using a scanning electron microscope (SEM, Quanta 250 FEI, Hillsboro, OR, USA), and the change in the surface topography as well as the roughness at scan size of 120 $µm^2$ was measured using an atomic force microscope (AFM, MFP-3D Origin+, Oxford Instruments, Santa Barbara, CA, USA) in a contact mode in air. The chemical composition of the surface film and its chemical state were determined using an X-ray photoelectron spectrometer (XPS, PHI 5600-ci, Physical Electronics, Chanhassen, MN, USA). XPS survey and high-resolution spectra were acquired at a detection angle of 45°, using a Kα line of a standard Al X-ray source operated at 300 W without charge neutralization. High-resolution curve fittings were determined using the least-squares method employing Gauss-Lorentz functions with a Shirley background subtraction. All peak positions were normalized to the C1 s peak, set at 284.5 eV. Additionally, a microwave plasma atomic emission spectroscopy (MP-AES, Agilent Technologies 4100/4200-torch system, Santa Clara, CA, USA) was used to perform additional chemical analysis of the electrolyte solution. This was mainly to verify the dissolution of Nb after the HEA specimens were subjected to polarization at 2 V for 2 h (PSP test) in the 0.5 M H_2SO_4 + 5 ppm F^- solution.

3. Results and discussion

3.1. Electrochemical characteristics

Over 1 h period of immersion in the 0.5 M H_2SO_4 solution with and

without 5 ppm F^- ions (Figs. 1a, 1b), the HEA specimens exhibited a slight drop in the potential, reflecting the dissolution of the primary passive film, before subsequently reaching a stable OCP, which indicates the stable passive film formation. On the contrary, the CP-Ti specimen experienced a remarkable drop in the potential that remained unchanged at a lower OCP value, indicating an extensive oxidation of Ti to Ti^{3+} in the acidic environment where over time its corrosion products further oxidize to Ti^{4+} [20,21]. The higher OCP values of HEA specimens indicate their superior corrosion resistance over CP-Ti. In the presence of F^- ions, all specimens showed lower OCP values compared to those in the 0.5 M H_2SO_4 alone, suggesting the effect of F^- ions in reducing the protectiveness of their passive film.

The EIS results, presented as Nyquist diagrams (Figs. 1c, 1e), show a similar semicircle feature for the three HEA specimens, confirming the passive film development on the alloy's surface [22]. The semicircle diameter size can directly relate to their corrosion resistance, where a larger diameter indicates higher corrosion resistance. For HEA specimens, in both 0.5 M H_2SO_4 solutions with and without 5 ppm F^- ions, the resistance increases with decreasing the Nb content, as confirmed later by an equivalent electrical-circuit analysis. Differently, the CP-Ti exhibited two capacitance semicircles, indicating a passive film that is not dense and susceptible to severe damage, which is more noticeable in the presence of F^- ions. Both semicircles appeared for CP-Ti correspond to specific behaviors manifested by two distinct maxima in the Bode diagram (Figs. 1d, 1f), pronounced in the phase-angle inverse Gaussian [21]. The first maximum, which appears in the high-frequency region, shows a significant intensity of the relaxation process, attributed mainly to the double-layer phenomenon. Such phenomena are generally linked to the formation and relaxation of the electrical double layer at the electrode-electrolyte interface, highlighting processes, such as charge transfer. However, the response in the low-frequency region may result from a combination of processes, including the dielectric properties of the film, which acts like a capacitor by polarizing under the effect of the applied alternating signal [23,24]. In addition, partial dissolution of the film can occur if it is unstable, or diffusion of electroactive ions through porous or defective regions leads to a variation in impedance.

For the HEA specimens, the Bode diagrams (Figs. 1d, 1f) show a constant phase angle at around – 81° over four decades of frequency [25], suggesting the presence of two-time constants that are not well separated. The resulting behavior tends to indicate a dominant capacitive response, a result of the combined effects of the double-layer capacitance and the dielectric properties of the passive film [25]. The impedance magnitude (|Z|) shows three distinct regions; in the frequency range from 100 kHz to 10 kHz, the electrolyte resistance dominated the response, representing purely resistive behavior. From 10 kHz to 0.1 Hz, the system exhibited capacitive behavior, characterized by a progressive slope corresponding to the capacitive contributions of the double layer and the passive film. Finally, from 0.1 Hz to 0.01 Hz, the impedance stabilized asymptotically, indicating a polarization resistance (R_p) where the system adopts a behavior dominated by the charge transfer process [26,27]. This R_p can be calculated from the total impendence of ω infinitely approaching zero using Eq. (1).

$$R_p = \lim_{\omega \to 0} \left(|Z|_{total} \right) \tag{1}$$

As the interface is not homogeneous, it behaves like a distribution of time constants, resulting in deviations from the ideal behavior of a capacitor. Typically, these deviations are modeled using constant-phase elements (CPEs) instead of ideal capacitors, to account for frequency dispersion. The impedance of CPE is:

$$Z_{CPE} = \frac{1}{Q \times (j\omega)^n} \tag{2}$$

where Q is the admittance of CPE, ω is the angular frequency, n represents the fitting exponent that ranges from 0 to 1, and j represents the imaginary unit. Therefore, the materials/solution interfaces can be modeled by means of an equivalent electrical circuit (Fig. 1g), where R_s is the electrolyte resistance in series with R_1 attributed to the inner layer other than resistance to charge transfer, in parallel with the first constant phase element CPE_1. And the second time constant attributed to the passive-film response modeled with R_2 and CPE_2 represents the film resistance and capacitance, respectively [28–30]. The R_p value of the CP-Ti is greatly lower than those of HEA specimens (Table 1), indicating the effect of Hf, Zr and Nb in improving the passivity of the formed passive film [31]. For the HEA specimens, their R_p values decrease as their Nb content increases. These R_p values are lower in the 0.5 M H_2SO_4 + 5 ppm F^- solution compared to those in the 0.5 M H_2SO_4 solution only, indicating the effect of F^- ions in weakening the protectiveness of the passive film. For the CP-Ti, the dramatic drop of R_p in the 0.5 M H_2SO_4 + 5 ppm F^- solution can be explained by the inverse relationship between R_2 and CPE_2 that indicates a breakdown of the protective film, which substantially reduces its corrosion resistance. This finding highlights the superior performance of the HEA compared to the CP-Ti in the aggressive 0.5 M H_2SO_4 + 5 ppm F^- solution [11].

In response to a potentiodynamic perturbation, the CP-Ti and three HEA specimens behave similarly under both solutions (Figs. 2a, 2b). The cyclic curves exhibit five main regions: active dissolution, primary passive transition, stable passive film, transpassive region, and anodic to cathodic transition. The specimens underwent a rapid anodic dissolution in the active region, where metal elements were oxidized to metal ions (M^{n+}) and released into the solution. This stage is characterized by a current rapid increase in density because of the absence of a protective layer. After this stage, the potential is increased to a higher value, confirming the initial growth of the passive film. A negative hysteresis was observed after the reverse scan, suggesting rapid recovery of the protective film and significantly lower current densities compared to the forward scan [32]. A slight decrease in the corrosion potential (E_{corr}) was observed in all specimens tested in the 0.5 M H_2SO_4 + 5 ppm F^- solution (Table 2), indicating a shift towards more negative potentials and suggesting an increased susceptibility to corrosion initiation. A sharp contrast in the corrosion current density (i_{corr}) was evident between the CP-Ti and HEA specimens, 805.11 μA.cm^{-2} for the CP-Ti compared to 0.92 μA.cm^{-2} for the $HEA_{0.2}$ in the 0.5 M H_2SO_4 + 5 ppm F^- solution, reflecting a better corrosion resistance of HEA specimens. The breakdown or pitting potential (E_b) shifted towards lower values in the presence of F^- ions, confirming its negative impact on the passive film. The values of i_{corr} and passivation current (i_{pass}) followed the order: $HEA_{0.2}$ > $HEA_{0.3}$ > $HEA_{0.4}$ > CP-Ti, a consistent trend with the results obtained from EIS.

Under a constant potential of 2 V recorded over 2 h (PSP test) in the 0.5 M H_2SO_4 + 5 ppm F^- solution, a noticeable progression towards passivity was observed for all tested specimens (Figs. 2c, 2d). Despite the aggressive nature of the F^- ions, known for facilitating localized corrosion by attacking protective oxide layers, the current density experienced an initial decrease in the first 100 s, suggesting a dynamic balance between the film formation and dissolution. Then, the current density remained low over the test period, implying a high corrosion resistance of the specimens during the steady-state operation. As observed in the last 1000 s of the experiment (Fig. 2d), the HEA specimens demonstrated a much lower stabilized current compared to the CP-Ti, with the $HEA_{0.2}$ stabilized at the lowest current density of about 7 μA.cm^{-2} whereas the CP-Ti reached a considerably higher value of 46 μA.cm^{-2}. These values were in perfect agreement with the values determined from the CPP experiment. Again, this finding indicates the superior protectiveness of the passive layer formed on HEA specimens over that on CP-Ti, allowing for a significantly lower current flow, which is a key indicator of the reduced corrosion activity of bipolar plates in PEMWE cells.

3.2. Surface characteristics

Under the SEM observation (Fig. 3), the CP-Ti surface shows evidence of severe corrosion that uniformly attacked over the entire

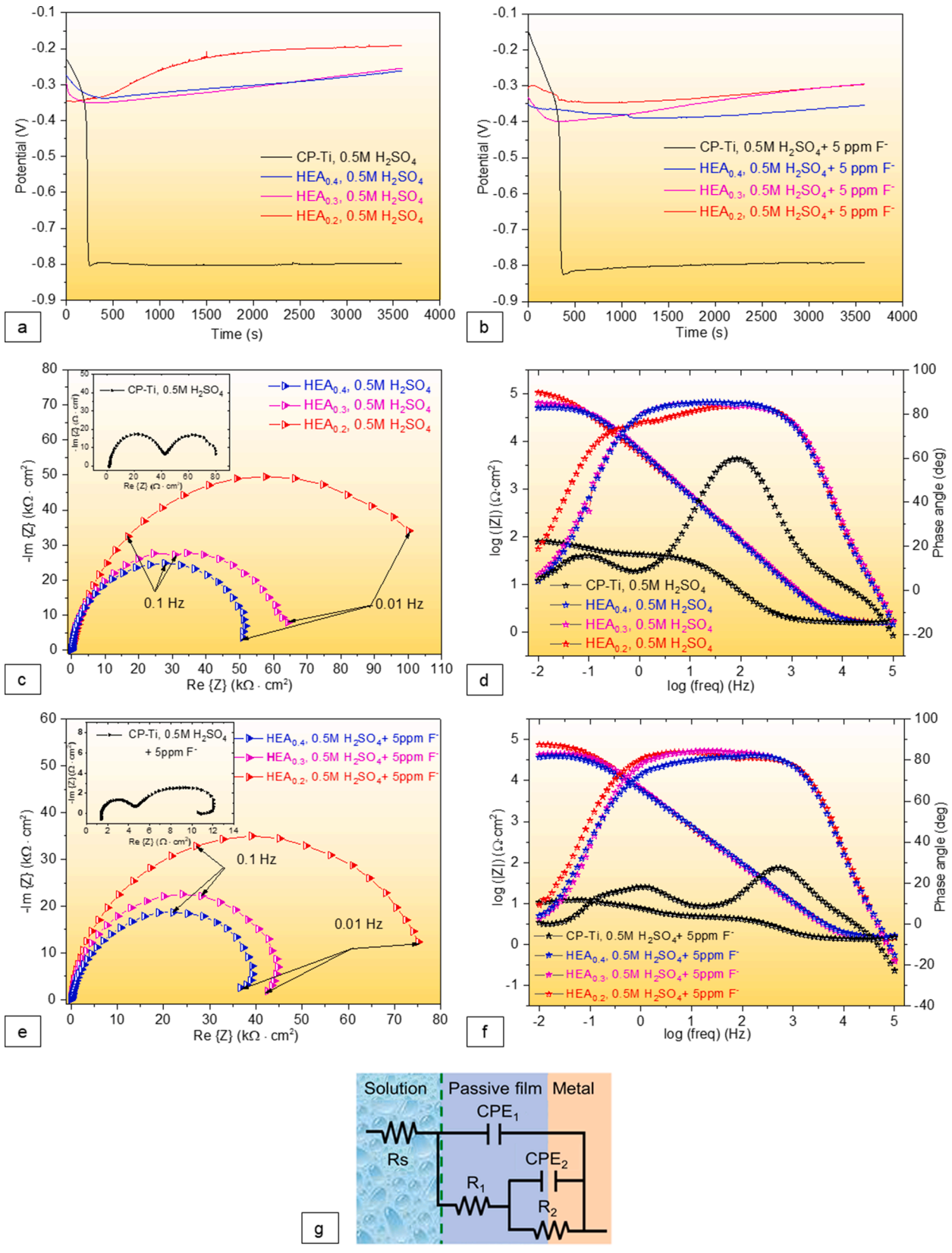

Fig. 1. Electrochemical characteristics of HEA and CP-Ti specimens: (a, b) OCP curves, (c, d, e, f) Nyquist and Bode diagrams, (g) proposed equivalent electrical circuit.

Table 1
EIS fitted parameters of CP-Ti and HEA specimens.

Specimen	R_S ($\times 10^{-3}$)	CPE_1	n_1	R_1	CPE_2	n_2	R_2	R_p	$\chi^2/\|Z\|$
In 0.5 M H_2SO_4									
CP-Ti	1.63	454.10	0.90	0.041	58.95	0.86	0.040	0.81	0.13
$HEA_{0.2}$	1.66	22.84	0.97	4.50	15.59	0.76	118.72	123.22	0.29
$HEA_{0.3}$	1.59	24.05	0.96	3.00	3.08	0.70	63.73	66.73	0.31
$HEA_{0.4}$	1.62	23.66	0.97	1.69	3.98	0.74	52.37	54.06	0.32
In 0.5 M H_2SO_4 + 5 ppm F^-									
CP-Ti	1.37	361.2	0.70	0.003	521.3	0.78	0.007	0.10	0.10
$HEA_{0.2}$	1.36	26.63	0.94	4.71	1.88	0.70	74.86	79.57	0.53
$HEA_{0.3}$	1.42	23.47	0.96	1.76	0.87	0.87	44.69	46.45	0.48
$HEA_{0.4}$	1.53	20.66	0.96	1.20	1.31	0.76	41.12	42.32	0.41

Note: R_s, R_1, R_2 and R_p in $k\Omega.cm^2$; CPE_1 and CPE_2 in $\mu F.s^{n-1}.cm^{-2}$; $\chi^2/|Z|$ indicates the accuracy of fitting.

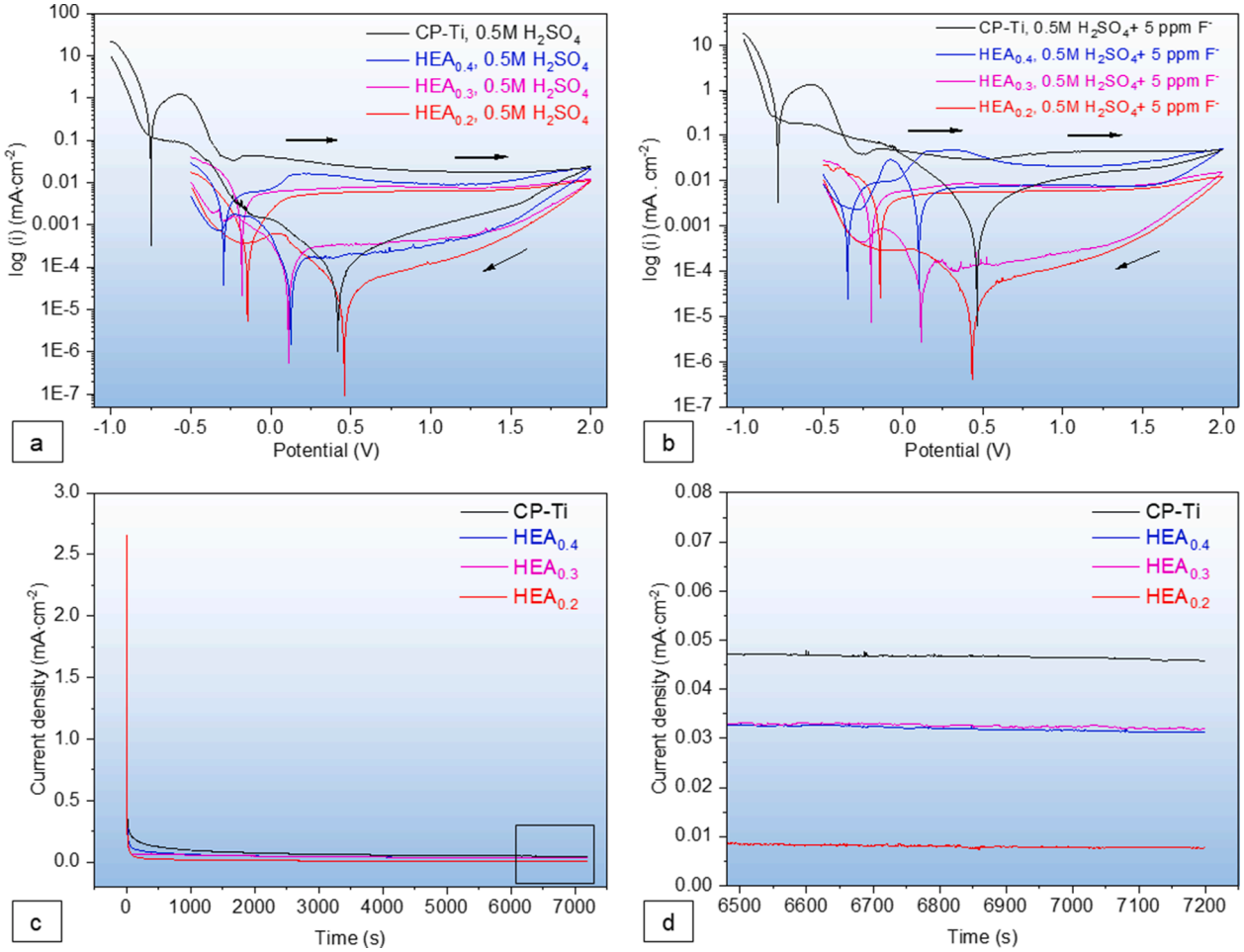

Fig. 2. Polarization behavior of CP-Ti and HEA specimens: (a, b) CPP curves in both solutions, (c, d) PSP curves in the 0.5 M H_2SO_4 + 5 ppm F^- solution.

surface, as well as pitting corrosion after being subjected to polarisation in the 0.5 M H_2SO_4 + 5 ppm F^- solution. In contrast, the HEA specimens show a negligible sign of corrosion, and an absence of visible pitting on their surface (Fig. 3f, 3g, 3h). This finding aligns with the negative hysteresis behavior observed in the CPP curves, confirming the ability of the passive film on HEA specimens to undergo self-repair once pitting corrosion has been initiated. Although the CPP curve of the CP-Ti also indicated a repassivation capability, pitting corrosion continued to progress to form larger pits (Fig. 3e).

Further surface analysis by AFM confirms an obvious increase in surface roughness after polarization (Fig. 4), which can be attributed to the oxidation of the metal elements [33]. Despite this increase in roughness, rapid repassivation could have occurred, allowing a protective layer to be maintained on the surface even in the presence of aggressive F^- ions. The protective behavior is further confirmed by the absence of distinct pitting features on the surface. However, in the case of $HEA_{0.4}$, a sign of corrosion was observed at the grain boundaries (Fig. 4b), suggesting that the grain boundaries in this alloy are more susceptible to localized corrosion in the given environment [34]. The average surface roughness (Ra) and the root mean square (RMS) roughness measured for each sample (Table 3) provide a quantitative insight into the surface changes induced during polarization. Note that AFM images for the CP-Ti after polarization cannot be obtained due to severe surface degradation (roughness) that rendered the AFM tips unable to accurately measure the roughness [35]. This extreme surface roughness underscores the inferior resistance of the CP-Ti to the

Table 2
Polarization curves fitted parameters of CP-Ti and HEA specimens.

Specimen	E_{corr} (mV)	i_{corr} (μA.cm^{-2})	i_{pass} (μA.cm^{-2})	E_b (mV)
In 0.5 M H_2SO_4				
CP-Ti	– 778.4	529.50	16.59	–
$HEA_{0.2}$	– 146.47	0.61	6.36	1258
$HEA_{0.3}$	– 178.01	1.41	7.47	1199
$HEA_{0.4}$	– 296.62	1.61	9.02	1062
In 0.5 M H_2SO_4 + 5 ppm F^-				
CP-Ti	– 779.53	805.11	44.90	–
$HEA_{0.2}$	– 139.43	0.92	6.03	1228
$HEA_{0.3}$	– 195.73	1.47	7.00	1008
$HEA_{0.4}$	– 344.50	1.80	21.18	948

Note: The breakdown potential (E_b) refers specifically to the onset of transpassive dissolution rather than the conventional initiation of pitting corrosion, and is identified at the potential where the current density begins to increase, marking the transition from passive film stability to active dissolution.

aggressive 0.5 M H_2SO_4 + 5 ppm F^- solution when compared to the HEA specimens.

Further analysis by the XPS reveal the chemistry of the native film prior to being subjected to the PSP test and the passive film after the PSP test. The XPS spectra revealed a formation of the oxides of Ti, Zr, Hf, and Nb on the passive film (Fig. 5), where the binding energies in both native and passive films are summarized in Table 4.

The deconvolution of XPS spectra of Ti 2p revealed two distinct peaks appeared at bending energies of 458 eV and 463 eV corresponding to Ti $2p_{3/2}$ and Ti $2p_{1/2}$, respectively (Fig. 5a), which are attributed to TiO_2 [36]. The oxidation of Ti to Ti^{4+} proceeds through an intermediate state, Ti^{3+}, as described by the following reactions [37]:

$$Ti + H_2O \rightarrow 2H^+ + 2e^- \quad (3)$$

$$2TiO + H_2O \rightarrow Ti_2O_3 + 2H^+ + 2e^- \quad (4)$$

$$Ti_2O_3 + H_2O \rightarrow TiO_2 + 2H^+ + 2e^- \quad (5)$$

The XPS spectra of Zr_{3d} were characterized by two peaks associated with ZrO_2 appearing at 182 eV for Zr $3d_{5/2}$ and at 185.4 eV are attributed to Zr $3d_{3/2}$ [38]. Although the latter peak could potentially be related to ZrF_4 [36], by its presence in the spectrum of the native film, it confirms that it originated exclusively from Zr $3d_{3/2}$, following these reactions [39]:

$$2Zr + H_2O \rightarrow Zr_2O + 2H^+ + 2e^- \quad (6)$$

$$Zr_2O + H_2O \rightarrow 2ZrO + 2H^+ + 2e^- \quad (7)$$

$$2ZrO + H_2O \rightarrow Zr_2O_3 + 2H^+ + 2e^- \quad (8)$$

$$Zr_2O_3 + H_2O \rightarrow ZrO_2 + 2H^+ + 2e^- \quad (9)$$

The XPS spectra for Hf confirmed its metallic state in the native film [40], while in the passive film it formed HfO_2 $4f_{7/2}$ at 17.0 eV and HfO_2 $4f_{5/2}$ at 19.0 eV [41]. No metallic states were detected for any of the alloying elements, indicating that the surface of the passive film was entirely in an oxide state. Therefore, it is predominantly in the form of Hf^{4+}, as indicated by these reaction steps [41]:

$$2Hf + H_2O \rightarrow Hf_2O + 2H + 2e^- \quad (10)$$

$$Hf_2O + H_2O \rightarrow 2HfO + 2H^+ + 2e^- \quad (11)$$

$$2HfO + H_2O \rightarrow Hf_2O_3 + 2H^+ + 2e^- \quad (12)$$

$$Hf_2O_3 + H_2O \rightarrow 2HfO_2 + 2H^+ + 2e^- \quad (13)$$

The XPS spectra of Nb were present exclusively in the $HEA_{0.4}$ passive film, through two distinct peaks at 207.9 eV for Nb_2O_5 $3d_{5/2}$ and at 210.9 eV for Nb_2O_5 $3d_{3/2}$ [42], formed through these reactions [37]:

$$Nb + H_2O \rightarrow NbO + 2H^+ + 2e^- \quad (14)$$

$$2NbO + H_2O \rightarrow NbO_2 + 2H^+ + 2e^- \quad (15)$$

$$2NbO_2 + H_2O \rightarrow Nb_2O_5 + 2H^+ + 2e^- \quad (16)$$

In contrast, no trace of Nb was detected in the passive film of $HEA_{0.2}$ nor $HEA_{0.3}$. This absence could be explained by the relatively low concentration of Nb on the surface of these alloys, as XPS principally analyzes elements in the outermost surface layers. If the surface or bulk concentration of Nb is insufficient, the signal may fall below the technique's detection threshold. Furthermore, the absence of Nb in the native film of $HEA_{0.4}$ suggests that surface reactivity is a key factor during electrochemical testing. A high affinity elements for oxygen, such as Ti, Zr, and Hf, dominate passive-film formation, reacting preferentially with oxygen and forming highly stable oxides, such as TiO_2, ZrO_2, and HfO_2 [43,44]. These oxides probably obscure the contribution of Nb to the passive film, making its detection difficult in alloys with a low Nb content. Thus, the presence of Nb in the passive film does not necessarily ensure superior corrosion resistance and may, in some cases, contribute to a more complex interaction of factors influencing the protectiveness of the passive film.

In all HEA specimens, HfO_2 remained the main component of their passive film, followed by ZrO_2 and TiO_2 (Fig. 5e). Accordingly, in terms of thermodynamics, the oxidation of Group IV elements (Hf, Zr, and Ti) is more advantageous than that of Group V elements (Nb and Ta) in refractory HEAs. Thus, the oxide growth rate adopted the following pattern: Hf > Zr > Ti > Nb [45].

Further semiconducting properties analysis of the passive film was performed by the Mott-Schottky technique to provide insights into the electronic structure and passive film stability formed after the PSP test (Fig. 5f). With this technique, the distribution of species charges at the film/electrolyte interface as a function of potential can be explained by measuring capacitance using the following equation [46].

$$\frac{1}{C^2} = \frac{2}{e\ \varepsilon_r\ \varepsilon_0 N}\left(E - E_{fb} - \frac{K_B\ T}{e}\right) \quad (17)$$

where C repersents the space charge capacitance of the passive film, e_0 is the elementary charge (1.602×10^{-19}C), N is defined as the density of the charge carriers (N_D: the electron donor concentration for an n-type semiconductor or N_A: hole-acceptor concentration for a p-type semiconductor), ε_0 is the vacuum permittivity (8.854×10^{-14} F/cm), ε_r denotes the dielectric constant of the film oxide, E is the applied potential, E_{bf} is the flat band potential, K_B is the Boltzmann constant (1.38×10^{-23} J/K), and T is the absolute temperature. Thus, the parameter, N_D or N_A, can be calculated from the slope of the linear part through this equation:

$$N_{D/A} = \frac{2}{e\ \varepsilon_r\ \varepsilon_0}\left[\frac{dE}{d\left(C^{-2}\right)}\right] \quad (18)$$

In addition, the ε_r can be determined via the logarithmic composition and mixture rule [47,48]:

$$ln\varepsilon_r = \sum V_i ln\varepsilon_i \quad (19)$$

where V_i and ε_i are related to the volume fraction and relative dielectric constant of the ith component, respectively. The constant of the oxides components were employed: $\varepsilon_{ZrO2} = 25$ [49], $\varepsilon_{TiO2} = 60$ [50], $\varepsilon_{HfO2} = 25$ [51], and $\varepsilon_{Nb2O5} = 42$ [52]. The volume fraction is assumed to be approximately equal to the atomic-percentage results found by the XPS analysis (Fig. 5e). Thus, the calculated ε_r for each specimen and its corresponding N_D were obtained (Table 5).

The Mott-Schottky plots of all specimens after the PSP test feature a linear region with a positive slope (Fig. 5f), indicating the n-type semiconductor nature of the formed passive film. The N_D values of the passive film fell in a range of 10^{21} to 10^{22} cm^{-3} orders of magnitude, with the highest value attributed to the CP-Ti. The same value was found in the literature for the pure Ti in the presence of F^-ions, confirming its

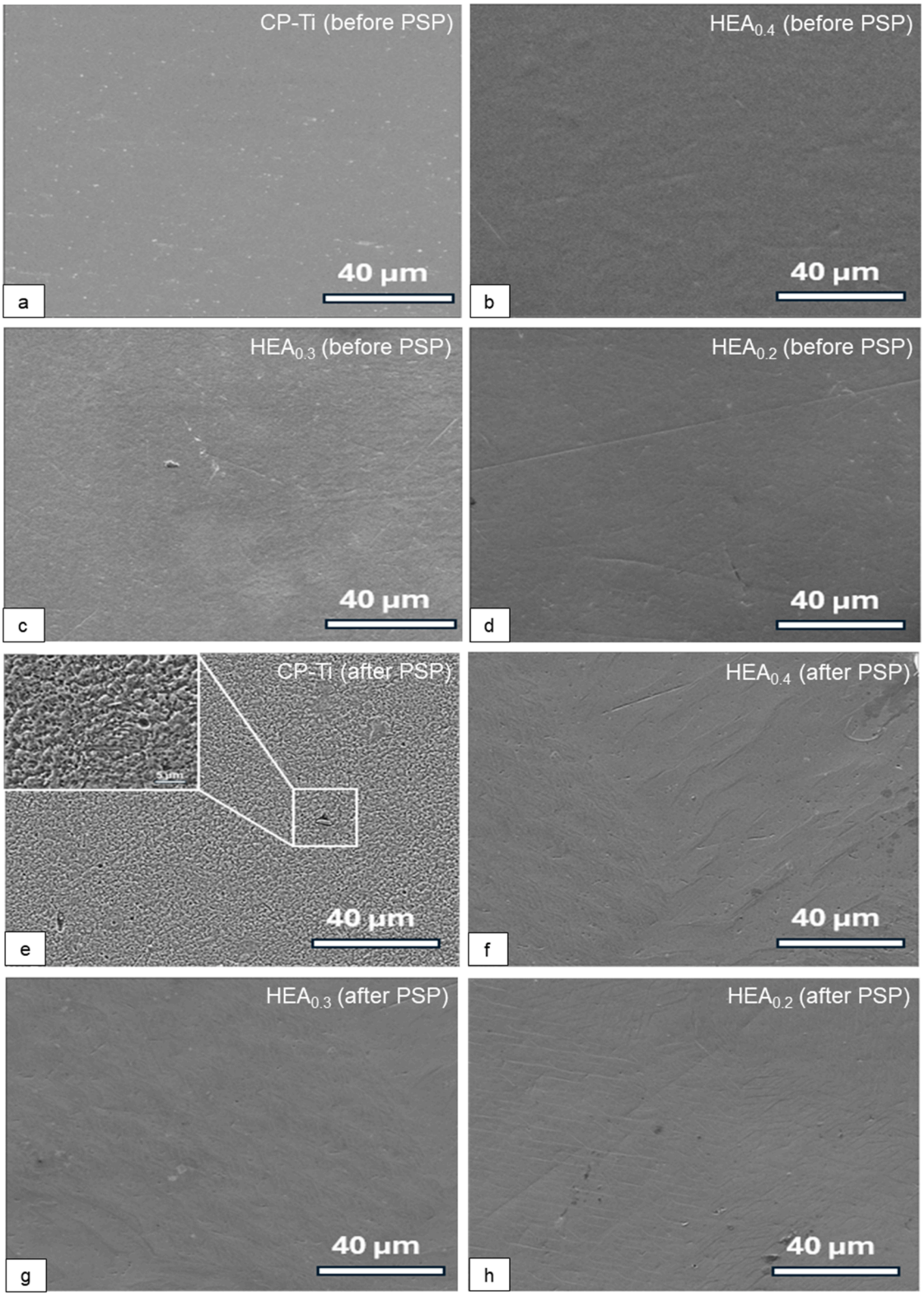

Fig. 3. SEM surface morphology of CP-Ti and HEA specimens before and after being subjected to the PSP test.

highly desorbed passive film [53]. The $HEA_{0.2}$ shows the lowest value, indicating the ability of its passive film to impede charge transfer. Based on the point defect model (PDM), oxygen ion vacancies are produced at the alloy/passive film interface. These vacancies will consequently reduced by the injection of oxygen ions from the electrolyte or the electrolyte/passive film interface [54]. In addition, F^- ions causes an increase in the number of free electrons in the passive film, thereby improving its conductivity. Therefore, the presence of F^- ions in the simulated conditions of PEMWE could have led to an increase in CP-Ti passive film carrier density, resulting in corrosion-resistance deterioration.

Further chemical analysis of the electrolyte solution confirmed the

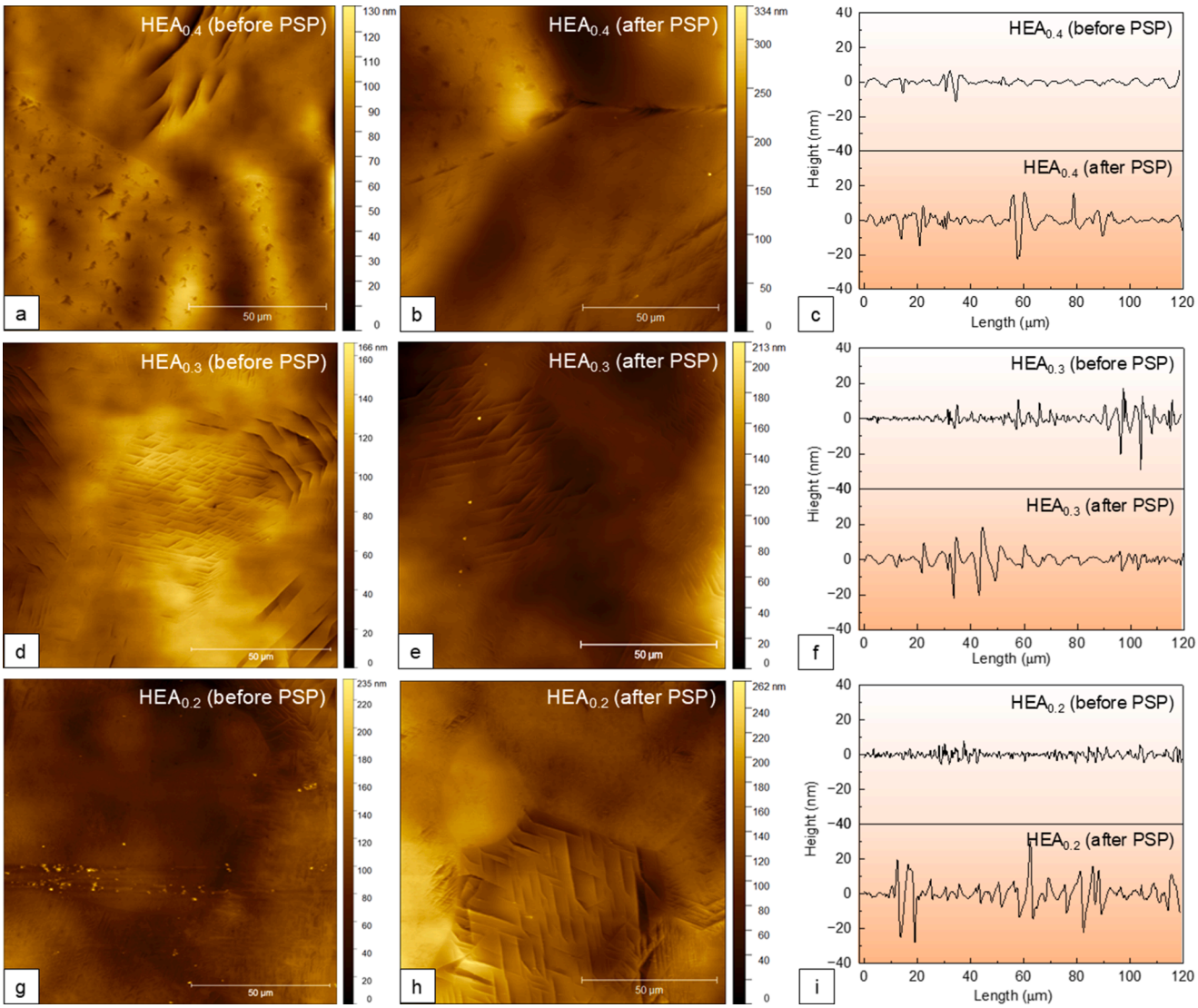

Fig. 4. AFM images of HEA specimens before and after being subjected to the PSP test alongside their surface roughness profiles.

Table 3
Surface roughness parameters determined from the AFM data.

Specimen	Before PSP test		After PSP test	
	Ra (nm)	RMS (nm)	Ra (nm)	RMS (nm)
$HEA_{0.4}$	1.336	1.896	2.639	4.387
$HEA_{0.3}$	2.103	3.577	2.702	4.218
$HEA_{0.2}$	1.427	1.831	2.172	3.215

dissolution of Nb ions from the passive film of HEA specimens after being subjected to the PSP tests (Table 6). During polarization, Nb underwent oxidation and then dissolved into the solution in an ionic form, with a higher dissolved amount detected for the $HEA_{0.4}$ specimen. The Nb_2O_5 is concentrated in the outer layer of the passive film but does not significantly enhance the corrosion resistance of the formed passive film [31,55], thus dissolved into the solution. The lower Nb concentration in $HEA_{0.2}$ and $HEA_{0.3}$ could have restricted its contribution to the formation of Nb_2O_5 in the passive film due to domination of higher stability oxides, particularly HfO_2 and ZrO_2 [43,44]. The Nb atoms competed with the stronger affinity for the oxygen of Ti, Zr, and Hf, which dominated the oxidation process during the passive-film formation, as evident from the XPS analysis (Fig. 5e). In $HEA_{0.2}$ and $HEA_{0.3}$, the Nb atoms are expected to be confined in deeper layers [31], thus prevented from dissolving into the solution.

3.3. Proposed corrosion mechanisms

The passive film formed on the surface of the CP-Ti in the solution without F^- ions exhibit a protective behavior due to a competition between the dissolution reaction and the formation of the oxide film. This process leads to the development of an inner dense layer, which protects the material from further dissolution. However, in the simulated condition of a PEMWE cell with the presence of F^- ions, the stability of this protective film is compromised, leading to a transformation of the dense oxide structure into a porous layer (Fig. 3e). This structural change significantly reduces the protective properties of the film, allowing aggressive ions to penetrate and accelerate corrosion processes. This phenomenon is clearly seen in the difference in R_p before and after the addition of F^- ions into the electrolyte (Table 1). Based on the theory of PDM, the formation of oxygen vacancies in the passive n-type film attracts F^- ions to occupy these vacancies and thus disrupt the film structure through the generation of localized positive cations that accelerate the ion-transport rate through the passive film towards the metal surface. Increased ions transfer facilitates the electrochemical dissolution of the Ti substrate, thereby weakening the protective properties of the passive layer. The XPS analysis of the passive film confirmed

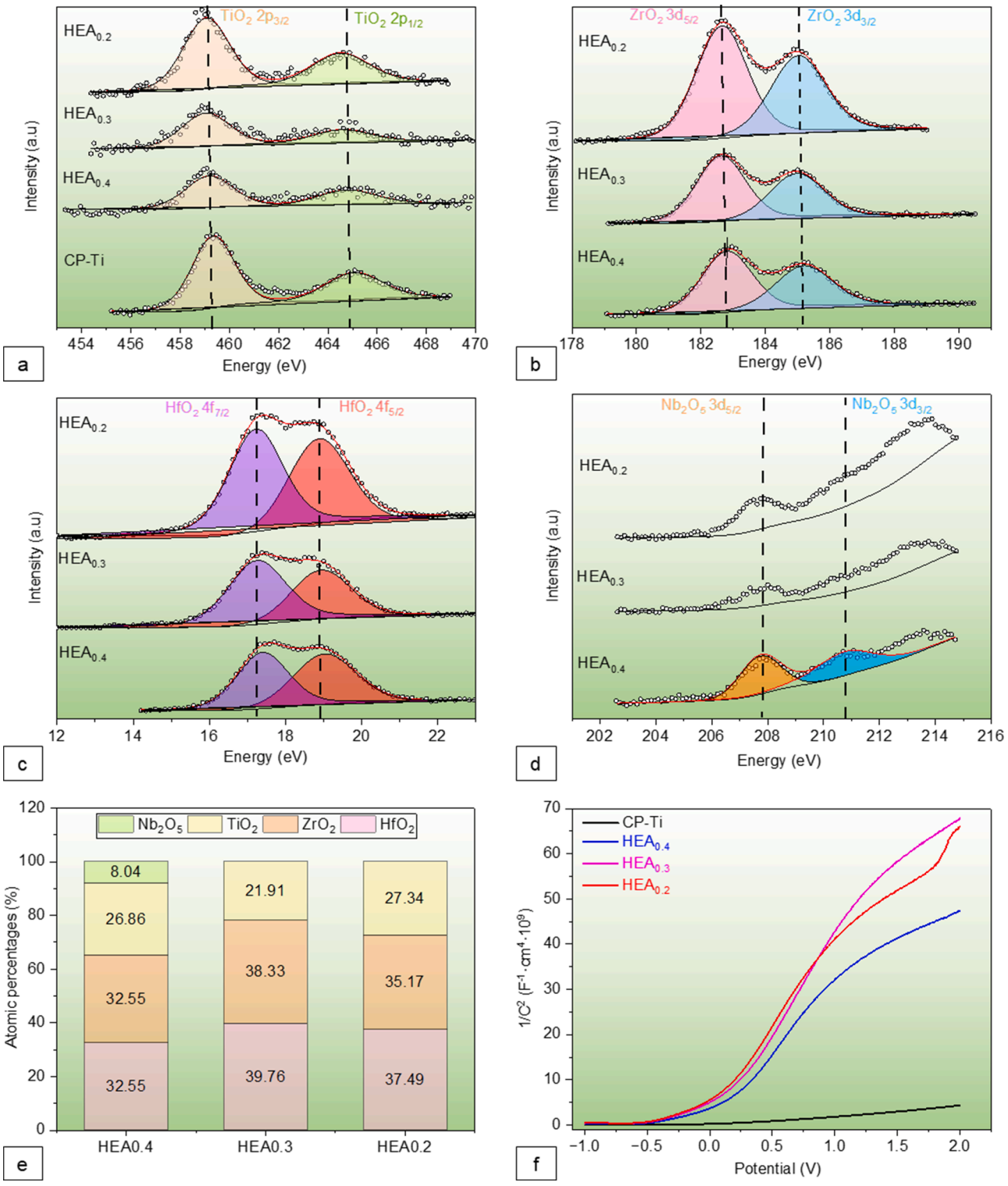

Fig. 5. Surface analysis results of CP-Ti and HEA specimens after being subjected to the PSP test: (a, b, c, d) XPS spectra of Ti, Zr, Hf, and Nb oxides detected on the passive film, (e) atomic percentage of oxides in the passive film, (f) Mott-Schottky plots.

the absence of TiF_6^{2-} or TiF_6^{3-} species (Table 4), which is consistent with the results of Li, et al. [56]. This observation can be credited to the high affinity of F^- ions to react with protons (H^+) at the interface under high-temperature conditions, in this case, 70 °C. This reaction leads to the formation of hydrofluoric acid (HF), a strongly aggressive compound that actively attacks the TiO_2-oxide film.

The synergistic effect of Hf, Zr, and Nb in influencing the corrosion resistance has been clearly demonstrated by the three HEA specimens. Hf and Zr contribute greatly to this improvement by promoting passivation, which is mainly attributed to their high adsorption for oxygen, which facilitates the formation of stable and protective oxide layers. Moreover, these elements have a low metal-to-metal bond strength, which favors the uniform distribution and incorporation of these oxides into the passive film, further enhancing its protectiveness. It has been well reported that the presence of Nb in the oxide-layer structure significantly improves the quality of the passive film [18]. This

Table 4
Binding energy and corresponding component in the native and passive film.

Specimen	Element	Photo electron lines	Oxidation state	Binding energy (eV)	
				Native film	Passive film
CP-Ti	Ti	$2p_{3/2}$–$2p_{1/2}$	Ti^{4+} (TiO_2)	458.41 - 463.33	459.33 - 465.03
$HEA_{0.4}$	Ti	$2p_{3/2}$–$2p_{1/2}$	Ti^{4+} (TiO_2)	458.63 - 463.99	459.17 - 464.77
	Zr	$3d_{5/2}$–$3d_{3/2}$	Zr^{4+}(ZrO_2)	182.61 - 185.0	182.80 - 185.18
	Hf	$4f_{7/2}$–$4f_{5/2}$	Hf(0), Hf^{4+} (HfO_2)	13.87 - 15.28 17.16 - 18.84	17.40 - 19.02
	Nb	$3d_{5/2}$–$3d_{3/2}$	Nb^{5+} (Nb_2O_5)	–	207.74 - 210.74
$HEA_{0.3}$	Ti	$2p_{3/2}$–$2p_{1/2}$	Ti^{4+} (TiO_2)	458.56 - 463.97	459.03 - 464.54
	Zr	$3d_{5/2}$–$3d_{3/2}$	Zr^{4+}(ZrO_2)	182.5 - 184.89	182.62 - 184.97
	Hf	$4f_{7/2}$–$4f_{5/2}$	Hf(0), Hf^{4+} (HfO_2)	13.77 - 15.21 17.05 - 18.73	17.25 - 18.93
	Nb	$3d_{5/2}$–$3d_{3/2}$	Nb^{5+} (Nb_2O_5)	–	–
$HEA_{0.2}$	Ti	$2p_{3/2}$–$2p_{1/2}$	Ti^{4+} (TiO_2)	458.60 - 463.97	459.05 - 464.49
	Zr	$3d_{5/2}$–$3d_{3/2}$	Zr^{4+}(ZrO_2)	182.47 - 184.84	182.64 - 185.01
	Hf	$4f_{7/2}$–$4f_{5/2}$	Hf(0), Hf^{4+} (HfO_2)	13.72 - 15.15 17.02 - 18.69	17.23 - 18.88
	Nb	$3d_{5/2}$–$3d_{3/2}$	Nb^{5+} (Nb_2O_5)	–	–

Table 5
The calculated ε_r values and their corresponding N_D.

Specimen	$HEA_{0.4}$	$HEA_{0.3}$	$HEA_{0.2}$	CP-Ti
ε_r	30.56	28.17	30.66	60
N_D ($\times 10^{20}$ cm^{-3})	1.58	1.43	1.20	10.9

Table 6
Nb ions concentration in the electrolyte solution after the PSP test.

Specimen	Ion concentration (ppm)
$HEA_{0.4}$	0.78
$HEA_{0.3}$	0.49
$HEA_{0.2}$	0.37

improvement can be attributed to the Nb ability to make covalent bonds with adjacent atoms through d-sharing [57], which contributes to the stability and integrity of the passive layer. Also, Nb can replace Ti in the TiO_2 oxide lattice due to their similar atomic radii [58]. This substitution acts as a crucial factor in improving corrosion resistance by effectively eliminating vacant anions in the TiO_2-network, thereby reducing defects [59,60]. This feature is supported by the XPS analysis (Figs. 5d, 5e, Table 4), which indicates the presence of Nb_2O_5 and an increase in the TiO_2 content in the $HEA_{0.4}$ passive film compared to the $HEA_{0.3}$, with a magnitude comparable to that observed in the $HEA_{0.2}$.

However, the present work indicates a small role of Nb toward passivation of HEAs in the acidic solution of the simulated PEMWE environment, contrary to the finding by Tanji, et al. in a neutral solution [18]. The Nb_2O_5 was absent on the top surface of the $TiHfZrNb_{0.2}$ and the $TiHfZrNb_{0.3}$ (Fig. 5e), yet their corrosion resistance is higher than that of $TiHfZrNb_{0.4}$, indicating that Nb could be a poor alloying element toward passivation. This behavior can be attributed to two main factors: first, the low concentration of Nb in these alloys may limit its ability to contribute significantly to the passive film; second, after the dissolution, Nb may not readily reattach to the surface as an oxide, as evidenced by its detected presence in the electrolyte solution (Table 6). It is also possible that Nb_2O_5 forms in the underlying layers of the passive film, rather than at the surface. In addition, the fluoride state of all Ti, Zr, Hf and Nb elements was not detected, probably not formed at all (Fig. 5, Table 4). It is possible that some fluorides were formed and then dissolved in the solution of 0.5 M H_2SO_4 to form HF gas.

4. Conclusions

In view of determining new materials for bipolar plates, the corrosion characteristics of $TiHfZrNb_x$ (x = 0.2, 0.3, and 0.4) high-entropy alloys (HEAs) have been thoroughly evaluated, in comparison to the CP-Ti, in 0.5 M H_2SO_4 + 5 ppm F^- solution at 70 °C that simulate the condition of PEMWE cells. The electrochemical performance of these HEAs purely relies on the nature of the formed passive film and the corrosive environment. The HEAs show a pseudo-passivation under open circuit potential conditions to a more noble potential, unlike the CP-Ti that was passivated to a lower potential. The formed passive layer on HEAs exhibits about 600 times higher polarization resistance than that of the CP-Ti, with the highest achieved at 79.57 kΩ.cm^2 for $TiHfZrNb_{0.2}$, leading to a sharp contrast in the corrosion current density, 805.11 μA.cm^{-2} for the CP-Ti vs. 0.92 μA.cm^{-2} for the $TiHfZrNb_{0.2}$, reflecting a far superior corrosion resistance of the HEAs. The synergistic effect of Hf, Zr, and Nb improves the corrosion resistance of HEAs by forming a dense passive film predominantly constituted of HfO_2, ZrO_2, and TiO_2, with a presence of Nb_2O_5 only on the $TiHfZrNb_{0.4}$. All passive films possess an n-type semiconducting characteristic with a much lower electron-donor concentration in the HEAs than in the CP-Ti. The absence of Nb_2O_5 on the top surface of the $TiHfZrNb_{0.2}$ and the $TiHfZrNb_{0.3}$ indicates a small role of Nb toward passivation in the aggressive acidic solution. Overall, the findings demonstrate the potential of $TiHfZrNb_x$ HEAs as alternative materials to titanium for durable and efficient bipolar plates in a PEMWE system.

Data availability

Data will be made available on request.

CRediT authorship contribution statement

Mariya Kadiri: Writing – original draft, Methodology, Investigation, Formal analysis, Conceptualization. **Ayoub Tanji:** Methodology. **Xuesong Fan:** Resources. **Peter K Liaw:** Writing – review & editing, Resources. **T M Indra Mahlia:** Writing – review & editing. **Hendra Hermawan:** Writing – review & editing, Validation, Supervision, Funding acquisition.

Declaration of competing interest

The authors declare that they have no known competing financial interests or personal relationships that could have appeared to influence the work reported in this paper.

Acknowledgments

The present work was funded by the Natural Sciences and Engineering Research Council of Canada (NSERC) via Discovery Grant (RGPIN-2023–03884) and Alliance International – Catalyst Grant (ALLRP 585698–23), and the “Réseaux québécois sur l’énergie intelligente” (RQEI) via the “projets pour la recherche inter ordres en hydrogène vert et en bioénergies”. Mariya Kadiri and Hendra Hermawan

gratefully thank Pascale Chevalier of the Center for Research on Advanced Materials (CERMA) for the assistance in the XPS analysis. Xuesong Fan and Peter K Liaw very much appreciate the support of (1) the Army Research Office Project (W911NF-13–1–0438 and W911NF-19–2–0049), (2) the National Science Foundation (DMR-1611180, 1809640, and 2226508), (3) the Department of Energy (DOE DE-EE0011185), and (4) the Air Force Office of Scientific Research (AF AFOSR-FA9550–23–1–0503).

References

[1] C. Le Quéré, R.M. Andrew, P. Friedlingstein, S. Sitch, J. Pongratz, A.C. Manning, J. I. Korsbakken, G.P. Peters, J.G. Canadell, R.B. Jackson, Global carbon budget 2017, Earth. Syst. Sci. Data 10 (2018) 405–448.
[2] M.F. Lagadec, A. Grimaud, Water electrolysers with closed and open electrochemical systems, Nat. Mater. 19 (2020) 1140–1150.
[3] S. Bouckaert, A.F. Pales, C. McGlade, U. Remme, B. Wanner, L. Varro, D. D'Ambrosio, T. Spencer, Net Zero By 2050: A roadmap For the Global Energy Sector, International Energy Agency, 2021.
[4] B.S. Zainal, P.J. Ker, H. Mohamed, H.C. Ong, I.M.R. Fattah, S.M.A. Rahman, L. D. Nghiem, T.M.I. Mahlia, Recent advancement and assessment of green hydrogen production technologies, Renew. Sustain. Energy Rev. 189 (2024) 113941.
[5] X. Luo, C. Ren, J. Song, H. Luo, K. Xiao, D. Zhang, J. Hao, Z. Deng, C. Dong, X. Li, Design and fabrication of bipolar plates for PEM water electrolyser, J. Mater. Sci. Technol. 146 (2023) 19–41.
[6] K. Ayers, High efficiency PEM water electrolysis: enabled by advanced catalysts, membranes, and processes, Curr. Opin. Chem. Eng. 33 (2021) 100719.
[7] T. Wang, X. Cao, L. Jiao, PEM water electrolysis for hydrogen production: fundamentals, advances, and prospects, Carbon Neutral. 1 (2022) 21.
[8] M. Prestat, Corrosion of structural components of proton exchange membrane water electrolyzer anodes: a review, J. Power. Sources. 556 (2023) 232469.
[9] S. Lædre, O.E. Kongstein, A. Oedegaard, H. Karoliussen, F. Seland, Materials for Proton Exchange Membrane water electrolyzer bipolar plates, Int. J. Hydrogen. Energy 42 (2017) 2713–2723.
[10] M.N.I. Salehmin, T. Husaini, J. Goh, A.B. Sulong, High-pressure PEM water electrolyser: a review on challenges and mitigation strategies towards green and low-cost hydrogen production, Energy Convers. Manage 268 (2022) 115985.
[11] H. Cheng, H. Luo, X. Wang, C. Dong, X. Li, Effect of fluoride ion concentration and fluctuating conditions on titanium bipolar plate in PEM water electrolyser environment, Corros. Sci. 222 (2023) 111414.
[12] S. Lædre, C.M. Craciunescu, T. Khoza, N. Vaszilcsin, A. Kellenberger, V. Bolocan, I. Mitelea, A. Ercuta, Issues regarding bipolar plate-gas diffusion layer interfacial contact resistance determination, J. Power. Sources. 530 (2022) 231275.
[13] S. Wu, W. Yang, H. Yan, X. Zuo, Z. Cao, H. Li, M. Shi, H. Chen, A review of modified metal bipolar plates for proton exchange membrane fuel cells, Int. J. Hydrogen. Energy 46 (2021) 8672–8701.
[14] N. Aukland, A. Boudina, D.S. Eddy, J.V. Mantese, M.P. Thompson, S.S. Wang, Alloys that form conductive and passivating oxides for proton exchange membrane fuel cell bipolar plates, J. Mater. Res. 19 (2004) 1723–1729.
[15] E.P. George, D. Raabe, R.O. Ritchie, High-entropy alloys, Nat. Rev. Materi. 4 (2019) 515–534.
[16] X. Yan, Y. Zhang, Functional properties and promising applications of high entropy alloys, Scr. Mater. 187 (2020) 188–193.
[17] Q. Zhang, K. Lian, G. Qi, S. Zhang, Q. Liu, Y. Luo, J. Luo, X. Liu, High-entropy alloys in water electrolysis: recent advances, fundamentals, and challenges, Sci. China Mater. 66 (2023) 1681–1701.
[18] A. Tanji, X. Fan, R. Sakidja, P.K. Liaw, H. Hermawan, Niobium addition improves the corrosion resistance of TiHfZrNbx high-entropy alloys in Hanks' solution, Electrochim. Acta 424 (2022) 140651.
[19] A. Tanji, X. Fan, R. Sakidja, P.K. Liaw, H. Hermawan, Role of niobium on the passivation mechanisms of Tihfzrnb high-entropy alloys in hanks' simulated body fluid, J. Funct. Biomater. 15 (2024) 305.
[20] J.J. Noël, N. Ebrahimi, D.W. Shoesmith, Corrosion of titanium and titanium alloys, in: K. Wandelt (Ed.), Encyclopedia of Interfacial Chemistry, Elsevier, Oxford, 2018, pp. 192–200.
[21] Z.B. Wang, H.X. Hu, Y.G. Zheng, W. Ke, Y.X. Qiao, Comparison of the corrosion behavior of pure titanium and its alloys in fluoride-containing sulfuric acid, Corros. Sci. 103 (2016) 50–65.
[22] O. Gharbi, M.T. Tran, M.E. Orazem, B. Tribollet, M. Turmine, V. Vivier, Impedance response of a thin film on an electrode: deciphering the influence of the double layer capacitance, Chemphyschem. 22 (2021) 1371–1378.
[23] D.S. Kong, Y.Y. Feng, Electrochemical anodic dissolution kinetics of titanium in fluoride-containing perchloric acid solutions at open-circuit potentials, J. Electrochem. Soc. 156 (2009) C283.
[24] L. Wang, M. Wang, M. Zhong, X. Li, Z. Cui, Degradation of thermal oxide film on pure titanium in an acidic environment containing fluoride, Npj. Mater. Degrad. 6 (2022) 65.
[25] R. Chelariu, G. Bolat, J. Izquierdo, D. Mareci, D. Gordin, T. Gloriant, R. Souto, Metastable beta Ti-Nb-Mo alloys with improved corrosion resistance in saline solution, Electrochim. Acta 137 (2014) 280–289.
[26] H. Liao, W. Watson, A. Dizon, B. Tribollet, V. Vivier, M.E. Orazem, Physical properties obtained from measurement model analysis of impedance measurements, Electrochim. Acta 354 (2020) 136747.
[27] Z.B. Wang, H.X. Hu, C.B. Liu, Y.G. Zheng, The effect of fluoride ions on the corrosion behavior of pure titanium in 0.05M sulfuric acid, Electrochim. Acta 135 (2014) 526–535.
[28] O. Gharbi, M.E. Orazem, M.T.T. Tran, B. Tribollet, M. Turmine, V. Vivier, On the graphical analysis of the impedance response of passive electrodes, in: ECS Meeting Abstracts MA2022-01, 2022, p. 1911.
[29] S.L.d. Assis, S. Wolynec, I. Costa, Corrosion characterization of titanium alloys by electrochemical techniques, Electrochim. Acta 51 (2006) 1815–1819.
[30] A. Barroux, J. Delgado, M.E. Orazem, B. Tribollet, L. Laffont, C. Blanc, Electrochemical impedance spectroscopy study of the passive film for laser-beam-melted 17-4PH stainless steel, Corros. Sci. 191 (2021) 109750.
[31] Z. Wang, Y. Yan, Y. Wu, X. Huang, Y. Zhang, Y. Su, L. Qiao, Corrosion and tribocorrosion behavior of equiatomic refractory medium entropy TiZr(Hf, Ta, Nb) alloys in chloride solutions, Corros. Sci. 199 (2022) 110166.
[32] Y. Qiu, S. Thomas, M.A. Gibson, H.L. Fraser, N. Birbilis, Corrosion of high entropy alloys, Npj Mater. Degrad. 1 (2017) 15.
[33] A. Motallebzadeh, Evaluation of mechanical properties and in vitro biocompatibility of TiZrTaNbHf refractory high-entropy alloy film as an alternative coating for TiO2 layer on NiTi alloy, Surf. Coat. Techn. 448 (2022) 128918.
[34] J. Czerski, M. Mitoraj-Królikowska, E. Godlewska, A. Wetzel, J. Witt, O. Ozcan, M. Marzec, M. Goły, Corrosion and passivation of AlCrFe2Ni2Mox high-entropy alloys in sulphuric acid, Corros. Sci. 229 (2024) 111855.
[35] J.R. Chen, W.T. Tsai, In situ corrosion monitoring of Ti–6Al–4V alloy in H2SO4/HCl mixed solution using electrochemical AFM, Electrochim. Acta 56 (2011) 1746–1751.
[36] J. Jayaraj, C. Thinaharan, S. Ningshen, C. Mallika, U.Kamachi Mudali, Corrosion behavior and surface film characterization of TaNbHfZrTi high entropy alloy in aggressive nitric acid medium, Intermetallics. 89 (2017) 123–132.
[37] R. Chelariu, L. Trinca, C. Munteanu, G. Bolat, D. Sutiman, D. Mareci, R. Souto, Corrosion behavior of new quaternary ZrNbTiAl alloys in simulated physiological solution using electrochemical techniques and surface analysis methods, Electrochim. Acta 248 (2017) 368–375.
[38] A.I. Karayan, S.W. Park, K.M. Lee, Corrosion behavior of Ti–Ta–Nb alloys in simulated physiological media, Mater. Lett. 62 (2008) 1843–1845.
[39] N. Stojilovic, E. Bender, R. Ramsier, Surface chemistry of zirconium, Prog. Surf. Sci. 78 (2005) 101–184.
[40] J. Jayaraj, K. Ravi, C. Mallika, U.Kamachi Mudali, Microstructure and corrosion behavior of Hf-40 wt pct Ti alloy in nitric acid medium for reprocessing applications, Metallurg. Mater. Trans. A 47 (2016) 4393–4403.
[41] N. Ohtsu, B. Tsuchiya, M. Oku, T. Shikama, K. Wagatsuma, X-ray photoelectron spectroscopic study on initial oxidation of hafnium hydride fractured in an ultra-high vacuum, Appl. Surf. Sci. 253 (2007) 6844–6847.
[42] S. Yu, J. Scully, Corrosion and passivity of Ti-13% Nb-13% Zr in comparison to other biomedical implant alloys, Corrosion 53 (1997) 965–976.
[43] L. Backman, J. Gild, J. Luo, E.J. Opila, Part I: theoretical predictions of preferential oxidation in refractory high entropy materials, Acta Mater. 197 (2020) 20–27.
[44] L. Backman, J. Gild, J. Luo, E.J. Opila, I.I. Part, Experimental verification of computationally predicted preferential oxidation of refractory high entropy ultra-high temperature ceramics, Acta Mater. 197 (2020) 81–90.
[45] P. Marcus, On some fundamental factors in the effect of alloying elements on passivation of alloys, Corros. Sci. 36 (1994) 2155–2158.
[46] D.B. Bonham, M.E. Orazem, A mathematical model for the influence of deep-level electronic states on photoelectrochemical impedance spectroscopy: II. Assessment of characterization methods based on mott-schottky theory, J. Electrochem. Soc. 139 (1992) 127.
[47] K. Wakino, T. Okada, N. Yoshida, K. Tomono, A new equation for predicting the dielectric constant of a mixture, J. Am. Ceram. Soc. 76 (1993) 2588–2594.
[48] T. Hanai, Theory of the dielectric dispersion due to the interfacial polarization and its application to emulsions, Kolloid-Zeitschrift 171 (1960) 23–31.
[49] D. Li, J. Wang, D. Chen, P. Liang, Influence of passive potential on the electronic property of the passive film formed on Ti in 0.1 M HCl solution during ultrasonic cavitation, Ultrason. Sonochem. 29 (2016) 48–54.
[50] V. Jovic, M. Barsoum, Corrosion behavior and passive film characteristics formed on Ti, Ti3SiC2, and Ti4AlN3 in H 2 SO 4 and HCl, J. Electrochem. Soc. 151 (2004) B71.
[51] G. He, L. Zhu, M. Liu, Q. Fang, L. Zhang, Optical and electrical properties of plasma-oxidation derived HfO2 gate dielectric films, Appl. Surf. Sci. 253 (2007) 3413–3418.
[52] J. Xu, L.L. Liu, Z.Y. Li, P. Munroe, Z.H. Xie, Niobium addition enhancing the corrosion resistance of nanocrystalline Ti5Si3 coating in H2SO4 solution, Acta Mater. 63 (2014) 245–260.
[53] Y. Wei, Z. Pan, Y. Fu, W. Yu, S. He, Q. Yuan, H. Luo, X. Li, Effect of annealing temperatures on microstructural evolution and corrosion behavior of Ti-Mo titanium alloy in hydrochloric acid, Corros. Sci. 197 (2022) 110079.
[54] D.D. Macdonald, The point defect model for the passive state, J. Electrochem. Soc. 139 (1992) 3434.
[55] Y. Zhang, Z. Wang, S. Huang, H. Liu, Y. Yan, Electrochemical behavior and passivation film characterization of TiZrHfNb multi-principal element alloys in NaCl-containing solution, Corros. Sci. 235 (2024) 112185.
[56] X. Li, L. Wang, L. Fan, M. Zhong, L. Cheng, Z. Cui, Understanding the effect of fluoride on corrosion behavior of pure titanium in different acids, Corros. Sci. 192 (2021) 109812.
[57] J. Li, S. Li, Y. Hao, H. Huang, Y. Bai, Y. Hao, Z. Guo, J. Xue, R. Yang, Electrochemical and surface analyses of nanostructured Ti–24Nb–4Zr–8Sn alloys in simulated body solution, Acta Biomater. 10 (2014) 2866–2875.

[58] G. Hautier, C. Fischer, V. Ehrlacher, A. Jain, G. Ceder, Data mined ionic substitutions for the discovery of new compounds, Inorg. Chem. 50 (2011) 656–663.
[59] L. Zheng, Q. Hua, X. Li, M. Li, Y. Qian, J. Xu, J. Zhang, Z. Zheng, Z. Dai, H. Zhang, Investigation on the effect of Nb doping on the oxidation mechanism of Ti3SiC2, Corros. Sci. 140 (2018) 374–378.
[60] D.M. Chen, G. Xu, L. Miao, S. Nakao, P. Jin, Sputter deposition and computational study of M-TiO2 (M= Nb, Ta) transparent conducting oxide films, Surf. Coat. Techn. 206 (2011) 1020–1023.